npj | biomedical innovations

Research

https://doi.org/10.1038/s44385-025-00026-w

Biochemical state in tissue can be detected through ultrasound signal

Kazuyo Ito[1,2,7,8] ✉, Yuta Iijima[3,7], Tomoki Misumi[4], Gen Hayase[5], Kazuki Tamura[6], Kenji Ikushima[1,2,8] ✉ & Daisuke Yoshino[1,2,8] ✉

Three-dimensional (3D) cell cultures, such as spheroids, are indispensable models for investigating cellular behaviors and responses under conditions that closely resemble in vivo environments. Conventional imaging techniques, including optical microscopy, are often limited by penetration depth, complicating the analysis of structural and biochemical changes within dense 3D systems. This study demonstrates the application of ultrasound imaging for the non-invasive evaluation of internal dynamics in cancer spheroids. Scattering-based acoustic parameters revealed spatial variations in amplitude and brightness density, correlating with cellular proliferation, apoptosis, and necrosis. Amplitude in central regions progressively decreased after Day 3, approaching near-zero by Day 15, reflecting necrotic core formation. Artificial inhibition of myosin contractility significantly influenced these patterns, providing insights into biomechanical contributions to spheroid organization. The findings establish ultrasound imaging as a label-free, high-penetration technique capable of addressing critical challenges in 3D culture analysis, offering new opportunities for studying cellular dynamics in spheroids and organoid models.

The importance of three-dimensional (3D) cell culture lies in its ability to closely emulate in vivo environment. Traditional two-dimensional (2D) cell culture systems, where cells are grown on flat, rigid surfaces, fail to replicate the complex structural and biochemical characteristics of natural tissue environments. Consequently, cellular behaviors, such as gene expression, metabolism, and drug responses, often diverge significantly from in vivo results, leading to limited clinical relevance[1–3]. In contrast, 3D cell culture systems, like spheroids and organoids, allow cells to interact in all dimensions, forming cell-to-cell and cell-to-matrix contacts that are essential for maintaining tissue-specific functions and accurately reflecting the microenvironment[4,5].

In recent years, various imaging techniques have been utilized for non-invasive observation of 3D cell culture models, such as spheroids, to assess their structural and functional dynamics[5]. Each method, including Optical Coherence Tomography (OCT), Förster Resonance Energy Transfer (FRET), and fluorescence microscopy, offers unique advantages and limitations that complement ultrasound's capabilities. OCT has an ability to illustrate time-dependent dynamics occurring in spheroids[6,7]. At cellular or even sub-cellular imaging was achieved. OCT, a powerful light-based imaging technique, enables high-resolution visualization of internal structures, making it ideal for detailed morphological assessments of 3D cell cultures. Due to its ability to penetrate deeper than traditional optical methods, OCT provides a valuable tool for non-invasive imaging of spheroid structures[7]. FRET is another highly specialized technique that provides insights at the molecular level, detecting energy transfer between closely situated fluorophores to reveal interactions between specific proteins or molecular structures[8]. This technique is especially valuable for studying biochemical processes, such as protein-protein interactions or conformational changes within cells, at a high level of specificity. FRET's ability to monitor molecular interactions in real time makes it a powerful tool for investigating cellular mechanisms that drive behavior in 3D models. Traditional fluorescence microscopy, like FRET, provides detailed information on cellular structures and protein localization, excelling in surface-level imaging with high specificity and resolution. This technique is widely used for its versatility and adaptability across various cellular and molecular applications. Many optical-based approaches have been proposed recently to capture more advanced information at sub-cellular scale[9]. For example,

[1]Department of Biomedical Engineering, Graduate School of Engineering, Tokyo University of Agriculture and Technology, Tokyo, Japan. [2]Division of Advanced Applied Physics, Institute of Engineering, Tokyo University of Agriculture and Technology, Tokyo, Japan. [3]Department of Food and Energy Systems Science, Graduate School of Bio-Applications and Systems Engineering, Tokyo University of Agriculture and Technology, Tokyo, Japan. [4]Department of Industrial Technology and Innovation, Graduate School of Engineering, Tokyo University of Agriculture and Technology, Tokyo, Japan. [5]Reseach Center for Electronic and Optical Materials, National Institute for Materials Science, Ibaraki, Japan. [6]Institute of Photonics Medicine, Hamamatsu University School of Medicine, Shizuoka, Japan. [7]These authors contributed equally: Kazuyo Ito, Yuta Iijima.[8]These authors jointly supervised this work: Kazuyo Ito, Kenji Ikushima, Daisuke Yoshino. ✉e-mail: itokazuyo@go.tuat.ac.jp; ikushima@cc.tuat.ac.jp; dyoshino@go.tuat.ac.jp

expanding on OCT, Optical Coherence Elastography (OCE) provides an added dimension by incorporating elasticity measurements, enabling researchers to assess the mechanical properties of 3D cultures, such as stiffness and elasticity variations[10]. These properties are critical for understanding cellular behavior and tissue-like responses, especially in models that simulate tumor microenvironments. OCE allows for localized assessment of stiffness gradients within the sample, providing insights into how mechanical cues influence cellular responses. Despite their distinct advantages, each of these optical-based imaging techniques has inherent limitations when applied to 3D cultured cell models. A primary constraint is limited penetration depth, as light scattering and absorption restrict the ability to capture detailed information from densely-packed cells. Fluorescence-based methods, including FRET and traditional fluorescence microscopy, suffer from phototoxicity and photobleaching, which hinder long-term imaging and may introduce artifacts that alter cellular behavior. OCT offers improved depth penetration but remains limited to a sub-millimeter scale, making it unsuitable for larger 3D structures such as millimeter-sized spheroids or organoids. The high-resolution imaging capability of confocal fluorescence microscopy is constrained by a shallow depth of field (DOF), which limits its ability to visualize deeper layers without complex z-stack reconstruction and extended imaging times. Additionally, fluorescence-based techniques often rely on exogenous labeling, requiring fluorophores or genetically modified cell lines, which can alter native cellular processes. These limitations highlight the need for alternative imaging modalities that offer deeper penetration, minimal invasiveness, and the ability to monitor structural and biochemical changes in 3D cell cultures without labeling.

Ultrasound (US) could be a suitable alternative because of its low-cost, label-free, and non-invasive imaging capability. It provides two-dimensional cross-sectional images, allowing real-time observation of the shape, boundaries, and internal structures of organs and tissues. It is frequently used for assessing fetal health and diagnosing abdominal organs such as the liver, kidneys, and gallbladder. Expanding applications from clinical to basic biological research, ultrasound technology has a great possibility to observe the internal changes occurring in the tissue or even within the cell. Ultrasonic imaging of spheroids possesses the significant advantage of being able to penetrate deep into the sample, allowing visualization of the internal structure of spheroids on the mm scale. Unlike optical-based imaging there are no limitations in the holding medium as long as the spheroid is anchored at the specific location. Another benefit of using ultrasound is the ability to conduct label-free observations without staining and fixation, thereby preserving the natural state of the cells and tissues under examination. This non-invasive approach minimizes the risk of altering cellular structures and functions, which is a common concern with traditional labeling and fixation methods. Indeed, some researchers succeeded in monitoring cell dynamics through ultrasound. Hagiwara et al. visualized changes in ultrasound amplitude with TGF-β1 stimulation to the living fibroblast cells[11]. Another report showed time-dependent changes in ultrasound absorption during mechanical stimulation to the cell nucleus[12]. The advantages of ultrasound, as demonstrated thus far, are particularly maximized in research involving three-dimensional cultured spheroids and organoids. In fact, the initial study conducted by Sherar successfully visualized the internal structures of tumor spheroids[13]. The resulting micrographs given by 100 MHz ultrasound reveal a striking contrast between the necrotic core and the viable rim of the spheroid, demonstrating the method's capability to provide tomographic images at depths up to 4 mm in biological specimens. Their study demonstrates the potential of ultrasound as a non-invasive technique for detailed imaging of the internal architecture of living tumor spheroids, paving the way for real-time structural analysis in complex 3D cell models.

This time, we investigate the internal changes of cancer spheroids created using a rapid cancer spheroid production method[14]. Briefly, this is a spheroid fabrication technique that utilizes the surface tension of a super-hydrophobic substrate and the gelation properties of collagen. This method allows for the efficient creation of uniform and reproducible spheroids, which are essential for consistent and reliable research outcomes. Ultrasound imaging was employed to observe cell-dynamics inside spheroids non-invasively and three-dimensionally. 20-MHz center frequency of ultrasound allows to depict the internal structure of the 2 mm radius of spheroid. This research leverages the amplitude of the ultrasound signal, correlating it with the brightness seen in B-mode ultrasound images. Employing established methods for validation, fluorescent images with immunostaining from the spheroid's center were also captured to monitor biochemical alterations.

The present article conducted two independent experiments assuming that biochemical changes inside the spheroid trigger the changes in the ultrasound signal; first, monitoring the internal state of the spheroids up to fifteen days post-formation, and second, observing changes in the internal state when actomyosin contractility is artificially inhibited. Blebbistatin (BLB) was used as the inhibitor of actomyosin contractility, and a group treated with DMSO alone was measured to control for the solvent's cytotoxicity. Previous studies have shown that the contraction of spheroids in the BLB-treated group is weaker compared to other groups. Therefore, we hypothesized that the amplitude values would follow a similar trend, with the control and DMSO groups showing similar patterns since their actomyosin contractility was not inhibited. We found the amplitude changes with successive cultivation days, and this trend matches with the fluorescent microscope observations. Notably, the amplitude showed dynamic changes starting from day 3, which marks the onset of the onset of spheroid contraction, and from day 11, when necrosis initiates at the center of the spheroid. The result also reveals this sequential change were disturbed with the inhibition of actomyosin contractility. These results indicate the potential of ultrasound imaging for the evaluation of internal biochemical changes in the spheroid without any destruction.

Results

Ultrasound has an ability of MDA-MB-231 cell dynamics observation within the fast fabricated spheroid

Figure 1 demonstrates the ability of ultrasound to observe the dynamics of MDA-MB-231 cells within the rapidly fabricated spheroid. Figure 1a illustrates the capability of ultrasound to inspect the internal changes of the spheroid in three dimensions. Figure 1b shows that during the early phase (days 1 and 2), the spheroid exhibited a homogeneous but sparse scatterer distribution. From days 3 to 9, as cellular density increased, the ultrasound scatter became densely packed. From day 11 onwards, a dense outer shell was observed, indicating the formation of a necrotic core. Figure 1c presents ultrasound-based volume changes with culture duration. Each spheroid exhibited various features depending on the cultured day. Rapid contraction of spheroids began on day 2 after fabrication (2.58 ± 0.30 mm^3 at day 1 and 2.17 ± 0.20 mm^3 at day2) and relaxed after day 3 (1.25 ± 0.11 mm^3), with the volume gradually decreasing until day 15 (0.47 ± 0.02 mm^3) (Fig.1c). Figures 1d, e display quantitative data averaged across each region of interest (ROI) located at every 20% distance from the center of the equivalent unit sphere, supporting these insights. During the early phase (days 1 to 2), the amplitude averaged over the spheroid was lower (0.30 ± 0.03 mV for day1 and 0.34 ± 0.03 mV for day2). From day 3 onwards, as the spheroid began to contract, the global amplitude increased drastically (0.50 ± 0.03 mV) and then gradually decreased over time. Region-dependent changes were also observed, with the amplitude decreasing more sharply at the center of the spheroid (R-1, R-2) compared to the periphery, where the decrease was more gradual (Fig. 1f). While little difference was seen between the inner and outer areas on Day 1 (0.30 ± 0.04 mV at R-1 (inner-most), and 0.34 ± 0.03 mV at R-4 (outer most)), the difference increased from Day 2 (0.51 ± 0.03 mV at R-1 (inner-most), and 0.60 ± 0.03 mV at R-4 (outer most))and became particularly pronounced from Day 7 onwards (0.27 ± 0.03 mV at R-1 (inner-most), and 0.51 ± 0.03 mV at R-4 (outer most)). In addition, the amplitude in the central areas R1 and R2 decreased rapidly from Day 3 onwards, and by Day 15 the amplitude were almost approaching 0. Conversely, the brightness density did not change drastically over the spheroid until day 11 regardless of the distance from the center (Fig. 1e, g). A substantial decrease in brightness density occurred in the later

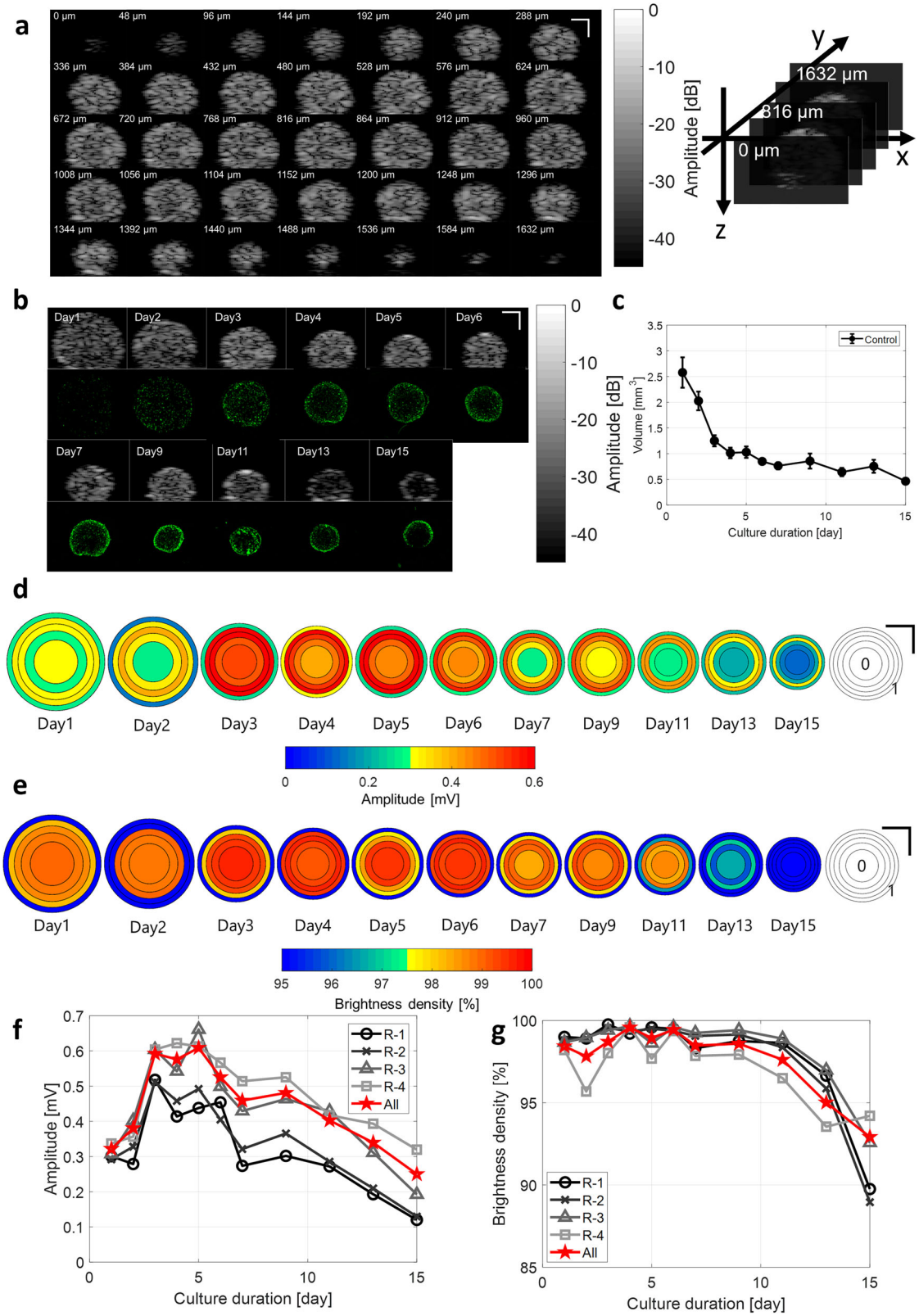

stages of incubation (days 13 and 15), particularly notable at the center of the spheroid (Fig. 1g).

Two ultrasound-derived parameters—amplitude and brightness density—were compared with the temporal profiles of five proteins: cleaved Caspase-3, HIF-1α, F-actin, phosphorylated myosin light chain (pMLC), and MMP-9 (Fig. 2a–d). Cleaved Caspase-3 and HIF-1α are associated with apoptotic activity and hypoxic response, respectively, while F-actin and pMLC are involved in cytoskeletal structure and contractility. MMP-9 is a matrix metalloproteinase related to extracellular matrix remodeling. In comparisons with Western blotting results (Fig. 2a, b), cleaved Caspase-3 and HIF-1α showed increased expression from Day 3 onward, accompanied by decreasing trends in both amplitude and brightness density. F-actin and

Fig. 1 | Acoustic observation of MDA-MB-231 cellular dynamics in the fast fabricated spheroid. a Amplitude (US B-mode) images of the entire spheroid on day 3. The top left image represents the left edge of the spheroid, while the bottom right image represents the right edge. The numbers within the images indicate the position of each respective slice within the entire spheroid. Scale bar = 500 μm. **b** Spheroid volume calculated based on the US B-mode images ($n = 3$, average±standard deviation in mm^3). **c** Time sequence of US B-mode images and GFP fluorescent image at each corresponding day at the center of each spheroid depicting internal changes in the process of its contraction. Each US B-mode image was log-compressed following to the normalization by the amplitude of the PDMS substrate. Scale bar = 500 μm. **d** Details of changes in the US B-mode images-based amplitude averaged across each region of interest (ROI) located at every 20% distance from the center of the equivalent unit sphere. The right-bottom panel represents the example of each ROI. Scale bar = 500 μm. **e** Details of changes in the US B-mode images-based brightness density averaged across each region of interest (ROI) located at every 20% distance from the center of the equivalent unit sphere. The right-bottom panel represents the example of each ROI. Scale bar = 500 μm. Changes in the (**f**) amplitude (in mV) and (**g**) Brightness density (in %) of US B-mode images averaged across entire spheroid (All), and averaged across each ROI located at every 20% distance from the center of the equivalent unit sphere. Circle symbols represent the most-proximal regions (i.e. R-1), cross and triangle symbols represent in between (i.e. R-2 and 3), and rectangle symbols represent the most-distal regions (i.e. R-4). Each dot on the chart represents the mean value, and the whiskers represent the standard deviation.

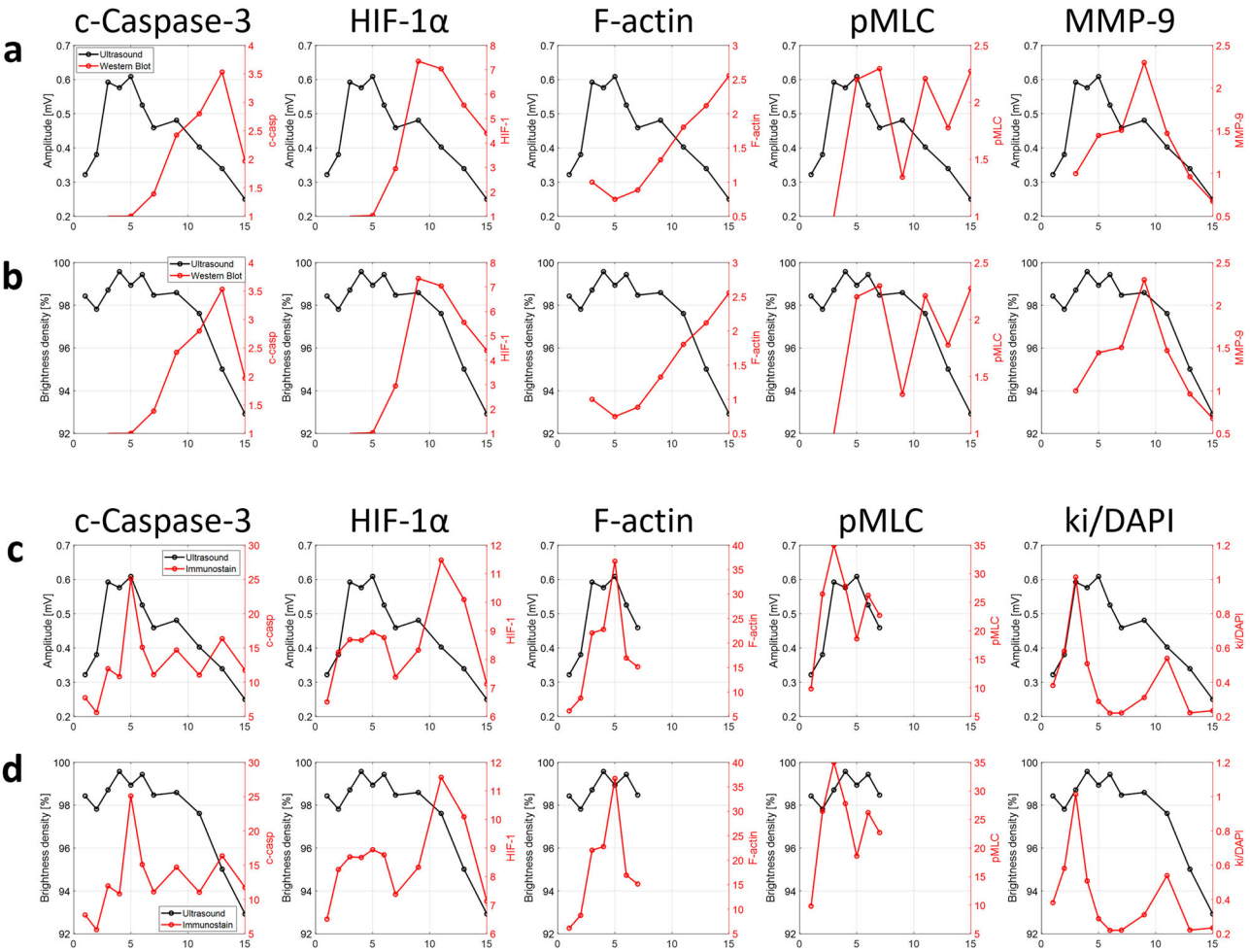

Fig. 2 | Culture-day dependent changes in protein expression and ultrasound-derived parameters assessed by immunohistochemistry and Western blotting. a, b Quantitative protein expression levels obtained from immunofluorescence imaging. **c, d** Protein expression levels obtained from Western blot analysis. In (**a**) and (**c**), the left y-axis indicates the expression levels of five proteins (cleaved-Caspase (c-Caspase)-3, hypoxia-inducible factor HIF-1α, F-actin, myosin light chain 2 phosphorylation (pMLC), and matrix metalloproteinase (MMP)-9, while the right y-axis represents the mean ultrasound brightness (amplitude) values. In (**b**) and (**d**), the right y-axis indicates the brightness density, defined as the number of signal-positive pixels per unit area, plotted against the protein expression of c-Caspase-3, HIF-1α, F-actin, pMLC, and ki-67 positive cells (ki/DAPI) (left y-axis). All parameters are shown as functions of culture day. Data are presented as mean ± standard deviation ($n = 3$). Both immunohistochemistry and Western blotting data was reproduced from our previous publication[17].

pMLC exhibited moderate variation over time, while MMP-9 displayed less consistent changes. Immunofluorescence staining was also performed to evaluate the spatial distribution of protein expression within spheroids, and the quantified intensities were compared with ultrasound-derived amplitude and brightness density (Fig. 2c, d). The expression of cleaved Caspase-3 and HIF-1α gradually increased from Day 3, particularly in the central regions of the spheroids. These spatial patterns corresponded with decreasing amplitude in the same regions. F-actin and pMLC signals also changed over time, showing region-dependent variations, while MMP-9 expression exhibited less distinct localization. On Day 5 in the control group, a radial gradient was observed in the B-mode image, with increased amplitude toward the spheroid periphery. A similar gradient was seen in the expression levels of several markers, particularly cleaved Caspase-3 and HIF-1α, which were elevated in the core region. These patterns are consistent with the structural layering of proliferating outer cells and apoptotic inner cells typically observed during spheroid maturation. The immunostaining data showed a general correspondence with ultrasound-derived spatial changes, particularly in signal attenuation in necrotic or hypoxic regions.

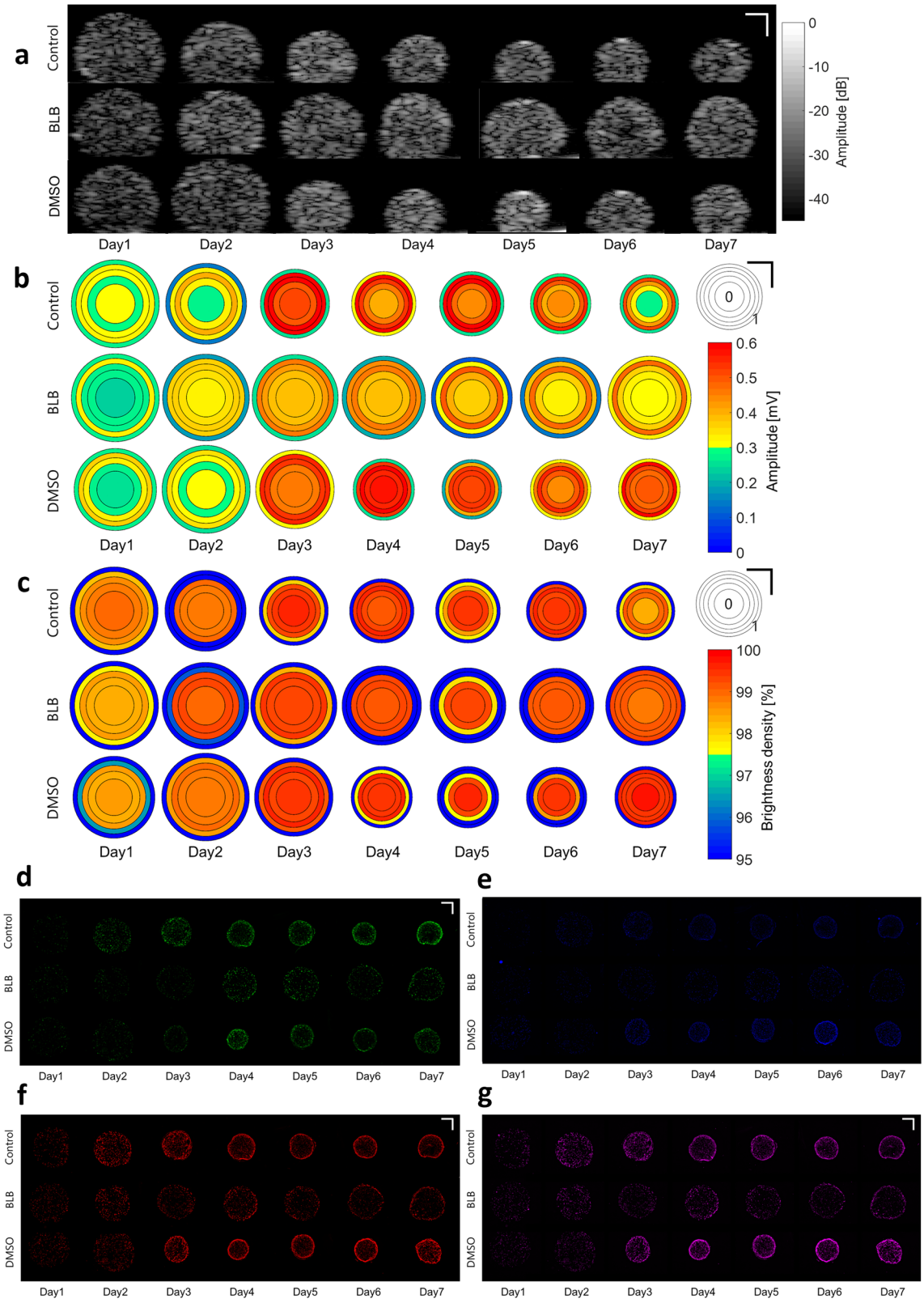

Ultrasound unveils the internal changes of spheroid caused by myosin inhibition

Next, we investigated the changes in amplitude when actomyosin contractility was artificially inhibited. Figure 3a shows the central cross-section of representative ultrasound B-mode images. As shown in Fig. 3, amplitude and size change with the number of days of culture. The control and DMSO groups exhibited similar trends. From day 3 onwards, the amplitude, particularly in the central region, increased significantly, corresponding to the rapid contraction of the spheroids. In contrast, the BLB-treated group showed similar amplitude to the other groups on days 1 and 2, but these values remained almost unchanged from day 3 onwards. The brightness density showed similar trends across all groups (Fig. 3c). Figure 3d–g

Fig. 3 | Changes in ultrasound images and immunohistochemistry caused by myosin inhibition with blebbistatin. a Time sequence US B-mode images depicting spheroid contraction under the condition of myosin inhibition with blebbistatin (BLB) (middle), and those without myosin inhibition with dimethyl sulfoxide (DMSO) (bottom). Top row represents control for comparison. Each US B-mode image was log-compressed following to the normalization by the amplitude of the PDMS substrate. Scale bar = 500 μm. **b** Details of changes in the US B-mode images-based amplitude averaged across each region of interest (ROI) located at every 20% distance from the center of the equivalent unit sphere. Top row shows the data from control group, middle row depicts the value with BLB, and bottom row depicts the value with DMSO. The top-right panel represents the example of each ROI. Scale bar = 500 μm. **c** Details of changes in the US B-mode images-based brightness density averaged across each region of interest (ROI) located at every 20% distance from the center of the equivalent unit sphere. Top row shows the data from control group, middle row depicts the value with BLB, and bottom row depicts the value with DMSO. The top-right panel represents the example of each ROI. Scale bar = 500 μm. Localization of GFP (**d**), DAPI (**e**), phosphorylation of MLC (**f**), and F-actin (**g**) in MDA-MB-231 spheroids. Scale bar, 500 μm. From left to right, each column shows each cultured day.

displays fluorescent imaging images. DAPI fluorescence was confirmed in the BLB group (Fig. 3e). Additionally, as shown in Fig. 3f and g, the expression of actin and phosphorylated myosin light chain (pMLC) was reduced in the BLB group.

To further elucidate the points demonstrated in Fig. 3, we observed that the expression levels of actin were similar across all three groups until day 2 of culture (Fig. 4a). From day 3 onwards, the control and DMSO groups showed an increase in actin expression, followed by a gradual decrease. This increase was particularly steep in the control group. In the BLB group, although actin expression also increased on day 3, the increase was more gradual, and subsequent changes were smaller compared to the other groups (Fig. 4a). The changes in amplitude, though exhibiting a smaller dynamic range than actin expression levels, followed a similar trend (Fig. 4b). As observed in the images, brightness density showed an upward trend from day 3 onwards, but there were no significant differences between the groups or across the culture days (Fig. 4c). Interestingly, the DMSO group displayed different results from the control group until day 2. The volume calculated from ultrasound images showed an inverse trend to that of the actin expression and amplitude (Fig. 4a, b). Although the volume in the BLB group decreased, it did so more gradually compared to the other two groups. The control and DMSO groups exhibited a rapid decrease in volume from day 2 onwards, reaching a plateau after day 4. The scatterplot of volume versus amplitude derived from ultrasound is shown in Fig. 4e. Two distinct groups could be identified: (1) a group with smaller volumes and higher amplitude, which included the control and DMSO groups from mid to late culture stages, and (2) a group with larger volumes and medium to low amplitude, which included all culture days of the BLB group and the early culture stages of the control and DMSO groups. Finally, we examined the region-dependent changes. While the overall trend was similar across all groups and regions, amplitude varied depending on the distance from the center. Notably, in the BLB group, the regions within 50% of the distance from the center showed similar trends regardless of the culture day. The difference in amplitude between the outer shell and inner shell was relatively large.

Discussion

The success of life science experiments often depends on the skill of the experimenter and the use of advanced instruments like confocal laser microscopes and flow cytometers, which require specialized expertise to operate. While these tools enhance our understanding of biological systems, they highlight the need for more accessible technologies that allow non-invasive real-time monitoring. Ultrasound (US) imaging, with its low cost, label-free, and non-invasive capabilities, offers a valuable alternative, particularly for observing three-dimensional cultured spheroids and organoids. This study with 20-MHz ultrasound demonstrated two key findings. Firstly, ultrasound has the capability to observe the internal dynamics of three-dimensional cultured cancer spheroids over time without labels. Secondly, it can differentiate changes in spheroid dynamics when myosin contractility is inhibited by blebbistatin. These findings indicate the effectiveness of ultrasound in monitoring internal changes within cancer spheroids, showing dynamic changes in amplitude that correlate with cell contraction and necrosis. Importantly, these findings, which agree with previous reports, were achieved without staining and non-destructively.

Ultrasound echo images are influenced by various physical phenomena, primarily reflection and scattering, that occur during the propagation of sound waves. Generally, when the echo source is significantly larger than the ultrasound wavelength, reflection occurs, whereas scattering occurs when the echo source is considerably smaller. In the case of the spheroids measured in this study, no scatterers larger than the wavelength exist within the structure, making scattering the dominant source. When scattering is the primary physical phenomenon, the echo signal comprises the summation of backscattered waves from point scatterers within the ultrasound-irradiated region. If point scatterers are densely packed within this region, the backscattered waves from each scatterer interfere with each other, causing the amplitude of the received echo signal to vary significantly depending on the interference state. This interference pattern results in a texture that is uncorrelated with the spatial distribution of the scatterers[15]. The changes in ultrasound backscatter intensity are related to a combination of intrinsic scatterer properties (i.e. acoustic impedance contrast between scatterer source and surrounding medium, scatter location, density, and size of the scatterer)[16]. Although these variations are often referred to as imaging artifacts, they are not necessarily regarded as unwanted noise in this context. Instead, they reflect the structural and compositional heterogeneity within the spheroid and are therefore interpreted as biologically meaningful signals. In clinical ultrasound practice, similar speckle patterns and attenuation profiles are routinely used for diagnostic purposes. Likewise, in this study, the textural and intensity variations observed in the echo images are considered to reflect the underlying biophysical properties of the sample, such as changes in cell density and intracellular organization.

From Fig. 1f, g, the results suggest that there are five distinct states throughout the entire culture period. During Days 1-2, the overall amplitude and brightness density are low, with minimal spatial variation as confirmed in Fig.1b, indicating State 1. On Day 3, we observe a maximum in amplitude (and possibly brightness density), which corresponds to State 2, as evidenced by the maximum Ki-67/DAPI ratio. Between Days 4-5, although the brightness density remains unchanged, the amplitude, signifying State 3. On a biochemical side, Ki-67 expression begins to decline, while c-Caspase-3 levels rise by Day 5, suggesting the initiation of apoptosis. During this period, the number of bright pixels remains constant, but the amplitude decreases. This suggests reduced interference due to a decrease in the number of scatterers within the resolution cell, as supported by the simulation results of Ohya et al[15]. State 4 (Days 6-11) reflects a hypoxic and nutrient-deprived central region, where cells begin to collectively migrate outward. This is supported by increased HIF-1α expression and a gradual rise in c-Caspase-3 levels. During this state, differences in both brightness density and amplitude start to emerge from the inner to outer regions. Although a necrotic core is not yet fully formed (Fig.1b), both amplitude and density begin to decline. Finally, state 5 (Days 13–15) is characterized by the formation of a necrotic core due to cellular swelling and rupture. The peak in c-Caspase-3 expression at Day 13 supports this interpretation, and the resulting reduction in acoustic impedance contrast leads to decreases in both amplitude and brightness density. From Day 3 onwards, despite no significant changes in volume, there are evident changes in amplitude and brightness density (Supplementary Fig. 1c–e), indicating that significant alterations within the spheroid are occurring, which are not reflected in volumetric changes.

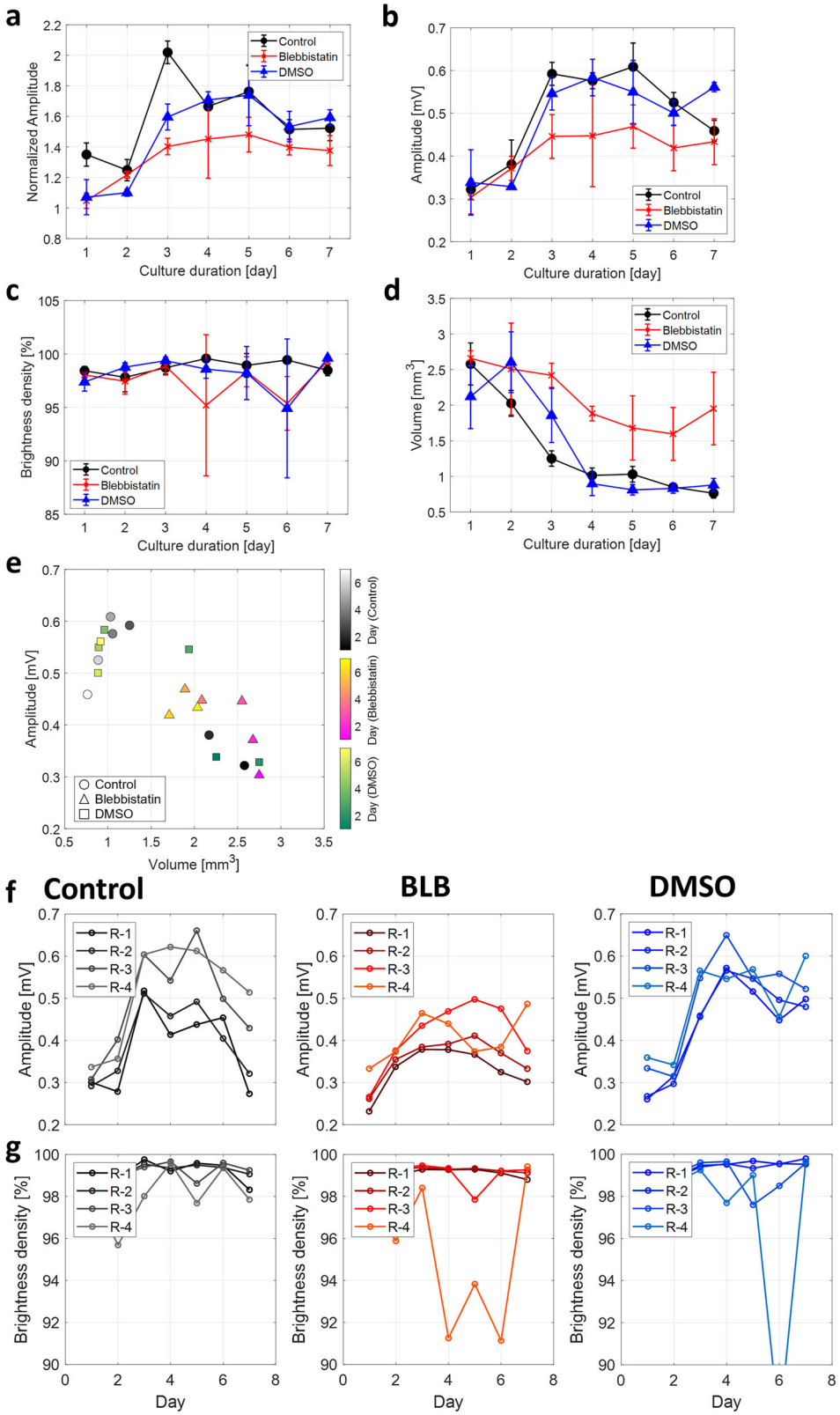

Fig. 4 | Myosin contractility inhibition causes the changes in the ultrasound brightness. a Relative expression level phosphorylation of myosin light chain 2 (pMLC) normalized by the intensity of DAPI staining in the 20% region from the center at day1. Changes in the (**b**) amplitude (in mV) and (**c**) brightness density (in %) of US B-mode images averaged across entire spheroid ($n = 3$). Both data were normalized by the intensity of US B-mode images in the 20% region from the center at day 1. **d** Spheroid volume calculated based on the US B-mode images. Each dot on the chart represents the mean value, and the error bar represents the standard deviation. Detailed changes in the US B-mode images based (**e**) amplitude (in) and (**f**) brightness density (in %) averaged across each ROI located at every 20% distance from the center of the equivalent unit sphere. From left to right, each graph represents control, BLB, and DMSO group, respectively. **g** Scatterplots comparing US amplitude and US-based spheroid volume (average value, $n = 3$). Circle, triangle, and rectangle markers represent control, BLB, and DMSO-treated groups, respectively. The color of the dot indicates the cultured day ranging from day 1 (black for control, magenta for BLB, and blue for DMSO) to day 7 (white for control, yellow for BLB, green for DMSO).

Regarding the biochemical changes during the spheroid culture process, our previous research with protein assays has provided some insights[17]. As the spheroids mature, the internal cell density increases, leading to hypoxia and subsequent HIF-1α expression. This process is followed by the development of a necrotic core at the center, along with the activation of Caspase-3. They further noted that tumor cells with high proliferative potential (Ki-67 positive cells) migrated to the outer layer of the spheroid as the culture period progressed. Considering these results in conjunction with the actual changes occurring within the spheroids, we can interpret the distinct states as follows: State 1 corresponds to the phase where cells are proliferating. During this phase, the distance between cells is relatively large, meaning the number of scatterers within the resolution cell is low, resulting

in low intensity and brightness density. State 2 marks the peak of cell proliferation (when Ki-67 expression is at its maximum), leading to a rapid increase in the number of scatterers within the resolution cell. State 3 occurs when the nutrients and oxygen necessary for cell proliferation can no longer reach the center of the spheroid, causing cells to begin dying from the center. Although these cells are dead, they are not removed, as confirmed by DAPI staining[17]. Consequently, the amplitude in the central region decreases, but the brightness density remains largely unchanged. The analysis did not reveal whether there was variability in the size of the cells near the center. State 4 indicates the onset of hypoxia in the center, prompting cells to begin collective migration from the inside to the outside. This results in increased amplitude at the periphery and decreased brightness density in the center due to the absence of cells. State 5 is characterized by the formation of a necrotic core (necrosis), where cells swell and rupture. This reduces the acoustic impedance difference with the surrounding area, leading to a decrease in both amplitude and brightness density.

In addition, immunohistochemical imaging revealed spatial and temporal variations in the expression of pMLC and F-actin, which were consistent with the changes observed in ultrasound brightness and brightness density. Combined with prior findings indicating that actin and myosin contribute substantially to acoustic impedance at the single-cell level[18], these results indicate that cytoskeletal components such as actin and myosin are likely to serve as key contributors to the echo signal in spheroid measurements. Based on these observations, both the number of cells per resolution volume and the intracellular cytoskeletal content are considered important factors influencing ultrasound brightness, providing support for the interpretations presented above.

However, discrepancies were observed between the results obtained from Western blotting and immunohistochemistry for several proteins. These differences is possibly attributed to the fundamental distinctions in measurement principles. Immunofluorescence offers spatially resolved localization of proteins, allowing visualization of their distribution within the tissue, whereas Western blotting involves bulk quantification from homogenized samples. As a result, Western blotting tends to reflect the characteristics of larger-volume regions, particularly the hypoxic or necrotic cores typically formed in the central area of spheroids. Moreover, because Western blotting requires multiple processing steps—such as protein extraction, electrophoresis, membrane transfer, and antibody incubation—it is more prone to artifacts including protein degradation or non-specific binding. These methodological differences should be taken into account when interpreting protein expression data. From an acoustic perspective, previous studies have shown that intracellular components such as the cytoskeleton, whole cells, and nuclei are key sources of scattering and impedance contrast in high-frequency ultrasound[19,20]. Further investigation using simulation and experimental validation will be required to quantify the relative contributions of these structures to ultrasound brightness in complex 3D cultures.

The amplitude of the ultrasound and the expression levels of actin showed similar trends (Fig. 4a, b), suggesting that the amplitude is related to myosin contractility. This correlation likely arises because the contraction of the spheroid increases the number of cells per unit area, thereby enhancing the number density of ultrasound speckles. This shift alters the interference state of the ultrasound, leading to an increase in amplitude. Notably, while the amplitude changed, the brightness density remained constant, indicating that cell contractility was modulated without inducing necrosis, consistent with previous studies. The stable brightness density further suggests that the proliferation function is maintained, indicating ongoing cellular activity. After Day 3, the brightness density was slightly lower in the BLB group compared to the control and DMSO groups, likely due to a reduction in the number of scatterers per unit area caused by the inhibition of contractility. Changes in amplitude from the center to the periphery followed similar trends as seen in the control group, although this effect was specific to the BLB group and differed from the control and DMSO groups, suggesting that the amplitude could serve as a marker to distinguish between these groups. Moreover, at the two-dimensional single-cell scale, previous studies based on optical tweezers have demonstrated that the addition of blebbistatin leads to changes in mechanical stiffness[21]. Force spectrum microscopy, also based on optical tweezers, has further shown that blebbistatin suppresses the random intracellular forces in the cytoplasm[22], a finding corroborated by similar trends observed in atomic force microscopy (AFM) analysis[23]. Additionally, OCT-based observations of spheroids have reported that blebbistatin induces cellular relaxation, increasing the fluidity of organelles within the cytoplasm[6]. Collectively, these findings align with our ultrasound data, supporting the notion that changes in actomyosin contractility due to blebbistatin administration can be effectively monitored through ultrasound, offering new insights into cellular dynamics within 3D spheroid models.

The results of this study demonstrate the applicability of ultrasound imaging for capturing internal biochemical and structural changes in spheroids, highlighting several advantages over existing optical-based techniques. One of ultrasound's primary strengths is its ability to achieve greater penetration depth, allowing for non-invasive visualization of internal structures that optical methods struggle to resolve. Unlike fluorescence-based techniques such as Förster Resonance Energy Transfer (FRET) and conventional fluorescence microscopy, which require staining or labeling, ultrasound imaging is inherently label-free, eliminating concerns related to phototoxicity, photobleaching, and potential disruptions to cellular function.

For example, Watanabe successfully clarified The mechanism of regulation of myosin II dynamics in vivo by phosphorylation of myosin regulatory light chain (MRLC) with the fluorescence-probe based approach demonstrating the phosphorylation-dependent regulation of myosin regulatory light chain (MRLC)[24]. However, fluorescence-based imaging required extensive labeling, which could potentially alter natural protein interactions and introduce artifacts. In contrast, ultrasound provides a non-invasive means of monitoring cellular organization, proliferation, migration, and apoptosis over extended culture periods or in response to external stimuli, such as drug treatments, without introducing exogenous labels. Additionally, while OCT and OCE typically require samples to be embedded in stabilizing matrices like hydrogels, ultrasound allows for imaging of free-floating samples, making it ideal for assessing dynamic responses to drug administration or environmental changes.

Previous studies using ultrasound have shown that various factors, such as cell size and cell viability, significantly contribute to changes in ultrasound intensity. At the microscopic scale, Fadhel et al. reported that acoustic impedance, which relates directly to the intensity of the received ultrasound signal, varies with cell size[25]. They also found that acoustic impedance differs between individual cells and cellular clusters, illustrating the impact of cellular structure on ultrasound properties. Additionally, studies have reported that acoustic intensity is affected by apoptosis[26]; this trend has been observed even in cells where apoptosis was artificially induced by drugs[18]. For aggregated cells (though not fully developed spheroids), one study demonstrated that the variance in cell size significantly contributed to the intensity of ultrasound echo signals[27].

In our measurements, a decrease in amplitude was observed in regions corresponding to necrosis (Fig. 1d, f), aligning with trends identified in earlier studies by Sherar[13]. In their study, three distinct regions were identified within spheroids: a low-backscatter outer ring consisting of live cells, a high-backscatter middle ring due to dead or dying cells, and a low-backscatter central region composed of necrotic cells. While our findings corroborate the lower backscatter in the necrotic core, the absence of a distinct high-backscatter intermediate layer in our results suggests possible differences in spheroid composition, cellular density, or imaging resolution between the studies. These discrepancies may arise due to variations in cell type, culture conditions, or methodological differences in ultrasound signal processing. Taken together, these findings suggest that ultrasound imaging has significant potential for evaluating the internal biochemical and structural changes occurring within spheroids, providing a scalable, label-free, and non-invasive approach for monitoring 3D culture models. However, further optimization of ultrasound parameters and comparative validation

against other imaging modalities are necessary to refine its applicability in diverse biological contexts.

One of the primary limitations of ultrasound imaging is its relatively low spatial resolution compared to these optical techniques. While high-frequency ultrasound improves resolution, this enhancement comes at the cost of penetration depth, limiting its applicability for imaging finer subcellular structures. In contrast, OCT and fluorescence microscopy achieve submicron resolution, allowing for detailed visualization of intricate structures within cells and enabling the study of localized molecular changes, which are essential for understanding cellular processes at a high level of detail. The trade-off between resolution and depth is also a limitation in ultrasound imaging, as achieving high resolution requires higher frequencies that reduce penetration depth, especially when imaging larger or more complex 3D samples. Given this trade-off, ultrasound is not expected to serve as a complete alternative to high-resolution optical modalities such as OCT or fluorescence-based techniques. However, by combining ultrasound with these complementary imaging approaches, it may be possible to overcome the individual limitations of each modality—achieving deeper tissue penetration while also preserving molecular and subcellular resolution where needed. Such integrative strategies could offer a more comprehensive and multiscale understanding of structural and functional dynamics in 3D cultured models.

Moreover, while ultrasound's label-free nature preserves cells in their natural state, it lacks the molecular tracking ability that labeled optical techniques achieve. Fluorescence microscopy, in particular, excels at highlighting specific molecules and structures, which allows for detailed monitoring of dynamic changes, molecular localization, and interactions within the cellular environment. This is particularly advantageous in studies involving specific cellular or molecular targets where direct labeling enhances observation accuracy. Although ultrasound is advantageous for long-term studies due to its non-invasive nature and absence of phototoxicity, it does not offer the same dynamic range of molecular insights as fluorescence-based techniques.

Further analysis including ultrasound scattering-based quantification, which is called quantitative ultrasound (QUS), is potentially able to address some of these limitations by providing additional information on cellular properties such as density, size, and organization[28,29]. Through QUS metrics, ultrasound can offer insights into mechanical and structural characteristics within 3D cell cultures, which may indirectly indicate cellular viability, proliferation, or structural changes in response to treatments. Leveraging ultrasonic scattering as an indicator may allow for the detection of phenomena smaller than the imaging resolution, potentially addressing spatial resolution limitations that have posed challenges in ultrasound diagnostics. By combining QUS with high-resolution, molecularly specific methods, researchers can achieve a more comprehensive view of cellular processes across spatial scales, providing depth and contextual insights that support a holistic understanding of 3D cell cultures and tissue models.

Nevertheless, as demonstrated so far, we were able to reveal the dynamic internal changes associated with spheroid maturation using ultrasound observation in a label-free and non-invasive manner. Previously, these dynamics could only be elucidated through time-consuming and technically demanding analytical methods such as immunostaining and western blotting. Our approach now allows for straightforward observation of these processes.

In conclusion, our study demonstrated that ultrasound imaging can effectively reveal the dynamic internal changes associated with spheroid maturation in a label-free and non-invasive manner. The amplitude of the ultrasound signal correlated with actin expression levels, indicating a relationship with myosin contractility. This relationship is likely due to changes in the interference state of sound waves caused by variations in cell density and contractility within the spheroid. The constant brightness density and variable amplitude suggest that while cell contractility changes, necrosis does not occur, maintaining cellular activity. Notably, the distinct trends in amplitude and brightness density changes between the BLB group and the control/DMSO groups highlight the potential of ultrasound imaging to differentiate these conditions. Thus, our findings suggest that ultrasound can be a powerful tool for observing changes in actomyosin contractility induced by blebbistatin, providing a simpler and more accessible method compared to traditional techniques like immunostaining and western blotting.

Methods

Cell culture and spheroid formation

Green fluorescent protein (GFP)-labeled MDA-MB-231 cells (human breast adenocarcinoma cell line, AKR-201, Cell Biolabs, San Diego, CA, USA) were cultured in a 75 cm^2 flask (VTCF75V, VIOLAMO, AS-ONE, Osaka, Japan) using Dulbecco's Modified Eagle Medium (DMEM; 31,600-034, Gibco, Thermo Fisher Scientific, Waltham, MA, USA) supplemented with 10% v/v heat-inactivated fetal bovine serum (S1810, Bio-West, Nuaillé, France) and 1% v/v penicillin–streptomycin (15,140-122, Gibco). Upon reaching 90% confluence, the cells were harvested using 0.25% trypsin–EDTA (25,200-072, Gibco) and resuspended in DMEM at a concentration of 5×10^7 cells/mL. Spheroid formation was conducted as per protocols previously established in our work [13]. A cell-suspended collagen solution [4.0 mg/mL; native collagen acidic solution (IAC-50, KOKEN, Tokyo, Japan), 10× DMEM, 10 mM $NaHCO_3$, 10 mM HEPES–NaOH (pH 7.5), and the cell suspension] was prepared on ice to achieve a final concentration of 5×10^6 cells/mL. This solution was then dispensed onto a superhydrophobic multiwell plate and incubated at 37 °C in a 100% humidified atmosphere with 5% CO_2 for 30–60 minutes. Following gelation, primary spheroids with diameters of 2 mm were transferred to a 48-well plate (VTC-P48, VIOLAMO). Molds for the spheroid fabrication were made by machining hemispherical holes with a radius of 1 mm (i.e., a diameter of 2 mm) on a superhydrophobic substrate. Although spheroids can be fabricated with size variation within ±20% (Iijima, 2024), minor variations in shape still exist. Therefore, for each culture day, approximately five spheroids were prepared, and three with the most ideal spherical morphology were selected for ultrasound measurements.

Spheroids were incubated under three independent conditions: Group 1: control, Group 2: cultured with (S)0(-)0Blebbistatin diluted with dimethyl sulfoxide (DMSO), and Group 3: cultured with DMSO. Spheroids in group 1 were incubated with no treatment. The spheroids were cultured from day 0, the day they were made, until day 15. Group 2 uses (S)-(-)-Blebbistatin (B592500, Toronto Research Chemicals (Toronto, ON, Canada)) to inhibit actomyosin contractility through the blockade of myosin II-dependent cellular processes[30]. To achieve inhibition of actomyosin contractility, MDA-MB-231 spheroids were incubated from day 0 in an experimental medium containing 5 μM blebbistatin, prepared with dimethyl sulfoxide (DMSO; Fujifilm Wako Pure Chemical Corporation, Osaka, Japan). Group 3 was act as a control for the group 2 considering the toxicity of the DMSO to the cell despite its negligible concentration. Spheroids in group 2 and 3 were cultured from day 0 until day 7. A total of 33 spheroids were used for Group 1, and 22 each were used for Groups 2 and 3. Three spheroids were selected for measurement on each measurement day (i.e. 11 Days x 3 = 33). After ultrasound measurement, the measured spheroid was not returned to the incubator, and new spheroid was selected from the incubator for measurement each time.

Ultrasound measurement

We designed a custom ultrasound laboratory scanning system and built it to acquire radio-frequency (RF) echo-signal data in three-dimensional from cultured spheroids. This system allowed spheroids to be scanned over their entire volume. The scanning apparatus featured a single-element, spherically focused, ultrasound transducer (PT20-6-12.7, Toray Engineering, Japan) with a 6.0-mm aperture length and 12.7-mm focal length. The transducer had a center frequency of 20.0 MHz and a -6dB bandwidth that extended from 4.1 MHz to 31.0 MHz. The axial resolution is calculated as 82.5 μm according to the relationship $c = f\lambda$ (c: speed of sound of the medium, f: frequency, λ: wavelength). The theoretically predicted beam diameter was 156.5 μm by using $BD = 1.02Fc/fD$ (F: focal length, D: aperture). The 6-dB depth of field was measured to be 1.60 mm extending

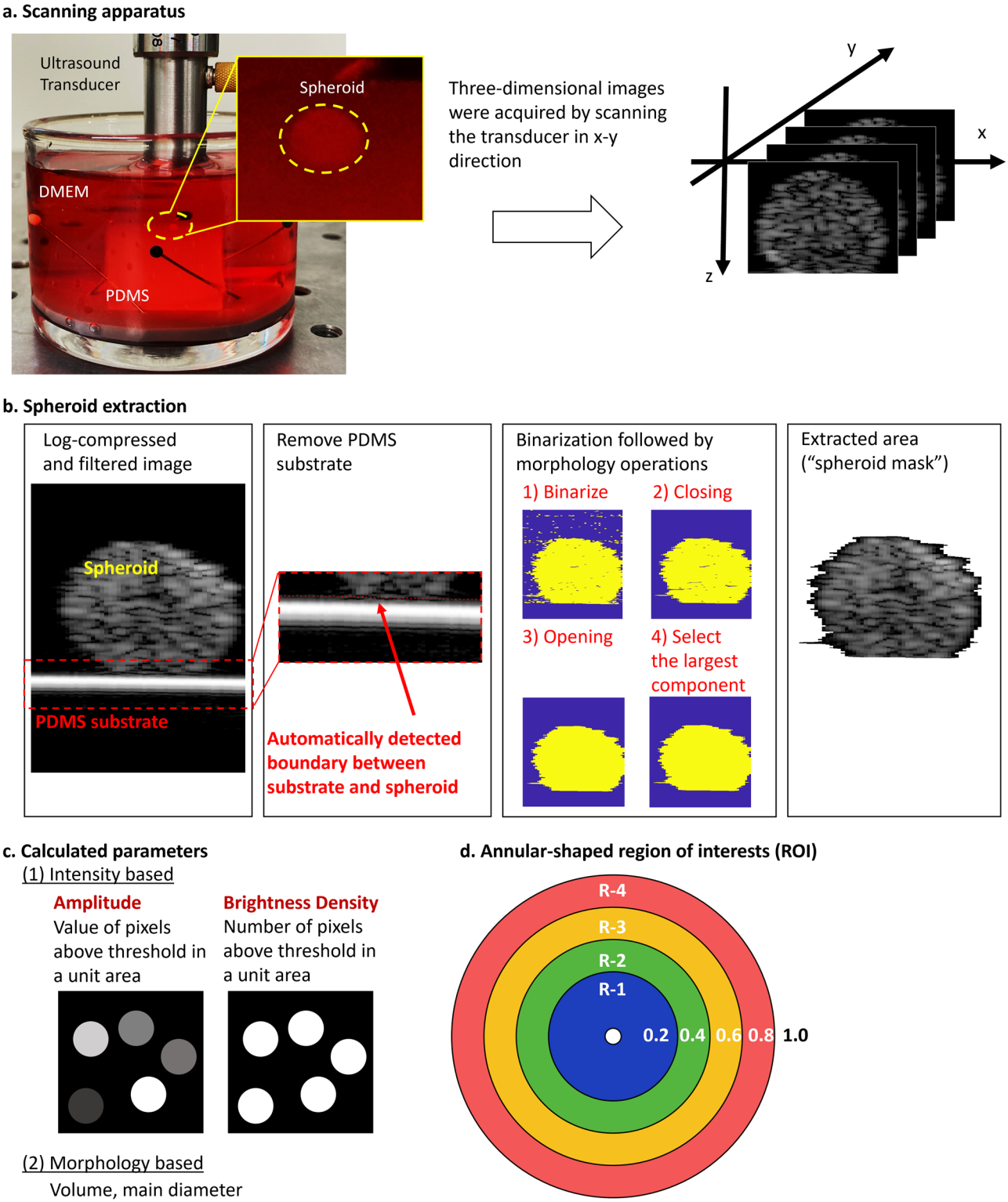

Fig. 5 | Data acquisition and post-processing. a Scanning apparatus with a spheroid. By scanning the ultrasound transducer in x-y direction, three-dimensional images were acquired and reconstructed. **b** Image-processing to extract spheroid from the image including log compression, PDMS substrate removal, binarization, and morphology operations. **c** Overview of the calculated parameters: Intensity-based and morphology-based parameters were calculated. **d** Schematic illustration of the annular-shaped region of interest (ROI)s. Taking the long axis of the ellipsoid as 1, the entire spheroid volume is divided into five parts in the radial direction (R-1: inner-most annuli, R-5: outer-most annuli). R-5 was removed because this marginal region possibly contains non-spheroidal information.

from 11.58 to 13.18 mm with the planer reflector measurement. The transducer was excited by a pulser/receiver unit (5073PR, Olympus) with 2 μJ of pulse energy, the pulse repetition frequency of 1 kHz and >2 ns of pulse width. RF echo signals were digitized with analog-to-digital converter (PXIe-5160, National Instruments) with 10-bit precision, 208 MHz sampling frequency.

Figure 5a illustrates the scanning apparatus. Each spheroid was placed in a water tank filled with DMEM and x40 diluted HEPES-NaOH to keep

pH during the measurement. In the water tank, the spheroid was placed on the PDMS substrate as an acoustic absorber. Mechanical scanning of the transducer in the X and Y direction acquired the three-dimensional RF echo signals (KXL06300-N2-G3). Scan vectors were uniformly spaced by 48 μm in X and Y directions across the entire scan volume to acquire complete full-volume 3D data from each spheroid. Each RF signal was averaged 100 times to increase the signal-to-noise-ratio. Sequential data acquisition from one spheroid finishes within 30 min. During the experiments, the focal depth was positioned below the apex of the spheroid. All measurement was conducted between 24.0–26.0 C°. Temperature of DMEM was measured before and after the measurement and used for the future speed of sound compensation.

Post-processing

Post-processing can be grouped into three steps: spheroid extraction, parameter calculation, and data summarization based on the distance from the center of the spheroid. Note that the evaluation of the signals was conducted using voltage data, while segmentation analysis was performed on log-compressed data to ensure an appropriate dynamic range. This approach allowed for accurate quantification of signal amplitude while maintaining reliable segmentation of the spheroid regions.

Acquired 3D radio-frequency signal were converted to voltage, followed by the filterization with a 0.1 to 35 MHz band-pass filter. This data has internal information from spheroid and was used for the subsequent evaluation ("voltage data"). Independently, to extract the echo signals originating from the spheroid and create a "spheroid mask," a series of signal and image processing steps were performed (Fig. 5b). First, the voltage data were log-compressed to ensure an appropriate dynamic range. Next, cross-correlation with a reference signal was applied to identify and remove echo signals originating from the PDMS layer, allowing for isolation of the spheroid region. The image was then binarized by a threshold that was equal to the average image intensity x4. Noise in the binary image that remained after thresholding was removed by opening and closing morphological operations using disk-shaped structuring element with a radius of 3 pixels. To remove other unwanted segments such as the anterior segment, only the largest connected component in the thresholded image was retained. Morphological operations were conducted to eliminate residual noise and refine the extracted spheroid mask.

For the regions identified as spheroids, two quantitative parameters were calculated as indicators (Fig. 5c). The first parameter, amplitude, represents the brightness value per unit area, expressed as the voltage signal. The second parameter, brightness density, was defined as the number of pixels per unit area that exceeded the noise level, regardless of their voltage values, and were therefore classified as signal-detected pixels. As morphological features of spheroids, main diameter and volume were calculated by ellipsoid approximation for the extracted spheroid volume data. For this estimated ellipsoid, five annular-shape regions of interest (ROI) were placed as a function of distance from the center (Fig. 5d, R-1: inner-most annuli, R-5: outer-most annuli). The boundary region, R-5, was excluded from subsequent analysis to account for the possibility that it may contain non-spheroidal information due to a segmentation error. Mean and standard deviation were calculated within each ROI. All processing was performed in MATLAB 2022a (The MathWorks, Natick, MA, USA) with the Image Processing Toolbox and Optimization Toolbox.

Immunohistochemistry

Cultured MDA-MB-231 spheroids were fixed with 4% paraformaldehyde phosphate buffer saline (PFA; 163–20,145, Fujifilm Wako Pure Chemical Corporation, Osaka, Japan) for 3 h at 4 °C. The spheroids were cryoprotected by soaking in 20 w/v% sucrose/phosphate buffered saline (PBS; 05913, Nissui Pharmaceutical, Tokyo, Japan) for 5 h and 30 w/v% sucrose/PBS for an additional overnight at 4 °C. Fixed spheroids were frozen in optimal cutting temperature compound (45,833, Sakura Finetek Japan, Tokyo, Japan) and cut into 10 or 15 μm-thick frozen sections on cryofilm using a cryostat (CM3050S or CM1860; Leica Microsystems, Wetzlar, Germany). After sectioning, the MDA-MB-231 cells were permeabilized with 0.1% Triton X-100 (17–1315-01, Pharmacia Biotech, Uppsala, Sweden) in Trisbuffered saline (TBS), followed by incubation in 1% Block Ace (BA; UKB40, DS Pharma Biomedical, Osaka, Japan) in TBS to prevent nonspecific antibody absorption. The cells were then stained using the primary and secondary antibodies diluted in 1% BA in PBS and PBS, respectively, at predefined concentrations. Cell nuclei and actin cytoskeleton were stained using 4′,6-diamidino-2-phenylindole dihydrochloride (DAPI; D1306, Invitrogen, Thermo Fisher Scientific) and Alexa Fluor 633 phalloidin (A22284, Invitrogen, Thermo Fisher Scientific), respectively. Stained MDA-MB-231 spheroid sections were observed using a fluorescence imaging system (THUNDER Imaging System, Leica Microsystems, Wetzlar, Germany). Independent of the acoustical evaluation, the feature extraction procedure was applied to the fluorescence microscope image but performed with the ImageJ plugin. The algorithm was presented in great detail in our previous paper[17]. The rate of Ki-67-positive cells (Ki-67/DAPI) was calculated by dividing the number of cells expressing Ki-67 by the total number of cells counted by cell nuclei. To provide a fair comparison between the different treatment, the amplitude of ultrasound and fluorescent microscopy images were both normalized by the control Day-1 from the control group.

Western blotting for quantitative analysis of protein expression

Western blotting was performed to evaluate the expression levels of cleaved-Caspase-3, HIF-1α, F-actin, and phosphorylated myosin light chain (pMLC) in spheroids. Protein lysates were prepared by lysing spheroids in buffer [50 mM Tris–HCl (pH 7.4), 150 mM NaCl, 1% Triton X-100, 1% SDS, 10 mM EDTA, 1 mM Na_3VO_4, 10 mM NaF, 20 mM DTT, and protease inhibitor cocktail], followed by centrifugation at 20,000 × g for 10 min at 4 °C. Supernatants were mixed with 4× Laemmli Sample Buffer and boiled for 5 min. Equal amounts of protein were separated via SDS-PAGE and transferred to PVDF membranes. Membranes were blocked with TBS containing 1% Blocking Agent and 0.05% Tween 20, then incubated with primary and secondary antibodies diluted in signal-enhancing buffer (Toyobo, NKB101). Immunoreactive bands were detected using Clarity Max ECL substrate. Protein band intensities were quantified using Image Lab software and normalized to loading controls (α-tubulin or β-actin).

Experimental reproducibility

All values are shown as mean ± standard deviation (SD) unless stated otherwise. Each data was obtained from three independently repeated experiments.

Data availability

The experimental data are available for research purposes from corresponding authors upon reasonable request.

Code availability

The scripts used for this study are available for research purposes from corresponding authors upon reasonable request.

Received: 8 January 2025; Accepted: 25 May 2025;
Published online: 13 June 2025

References

1. Birgersdotter, A., Sandberg, R. & Ernberg, I. Gene expression perturbation in vitro—a growing case for three-dimensional (3D) culture systems. *Semin. Cancer Biol.* **15**, 405–412 (2005).
2. Cukierman, E., Pankov, R. & Yamada, K. M. Cell interactions with three-dimensional matrices. *Curr. Opin. Cell Biol.* **14**, 633–640 (2002).
3. Nelson, C. M. & Bissell, M. J. Of extracellular matrix, scaffolds, and signaling: tissue architecture regulates development. *Homeost., Cancer* **22**, 287–309 (2006).
4. Yamada, K. M. & Cukierman, E. Modeling tissue morphogenesis and cancer in 3D. *Cell* **130**, 601–610 (2007).

5. Costa, E. C. et al. 3D tumor spheroids: an overview on the tools and techniques used for their analysis. *Biotechnol. Adv.* **34**, 1427–1441 (2016).
6. Scholler, J. et al. Dynamic full-field optical coherence tomography: 3D live-imaging of retinal organoids. *Light Sci. Appl.* **9**, 140 (2020).
7. El-Sadek, I. A. et al. Three-dimensional dynamics optical coherence tomography for tumor spheroid evaluation. *Biomed. Opt. Express* **12**, 6844–6863 (2021).
8. Kamioka, Y. et al. Live imaging of protein kinase activities in transgenic mice expressing FRET biosensors. *Cell Struct. Funct.* **37**, 65–73 (2012).
9. Lee, M. J. et al. Long-term three-dimensional high-resolution imaging of live unlabeled small intestinal organoids via low-coherence holotomography. *Exp. Mol. Med.* **56**, 2162–2170 (2024).
10. Mowla, A. et al. Multimodal mechano-microscopy reveals mechanical phenotypes of breast cancer spheroids in three dimensions. *APL Bioeng.* **8**, 36113 (2024).
11. Hagiwara, Y. et al. Ultrasonic intensity microscopy for imaging of living cells. *Ultrasonics* **49**, 386–388 (2009).
12. Fujiwara, N. et al. Development of a focused-ultrasound spectroscopic-imaging system combined with optical imaging for applying mechanical stimulation on living cells and the possibility of selective stimulation for the nucleus. *Jpn. J. Appl. Phys.* **63**, 63–68 (2024).
13. Sherar, M. D., Noss, M. B. & Foster, F. S. Ultrasound backscatter microscopy images the internal structure of living tumour spheroids. *Nature* **330**, 493–495 (1987).
14. Hayase, G. & Yoshino, D. CNC-milled superhydrophobic macroporous monoliths for 3D cell culture. *ACS Appl. Bio Mater.* **3**, 4747–4750 (2020).
15. Ohya, A., Yuta, S. & Nakajima, M. Quantitative analysis of ultrasonic speckle region-Scatterers' density and speckle region. *Jpn. J. Med. Ultrason.* **16**, 303–312 (1989).
16. Lizzi, F. L. Theoretical framework for spectrum analysis in ultrasonic tissue characterization. *J. Acoust. Soc. Am.* **73**, 1366 (1983).
17. Iijima, Y. et al. Biological characterization of breast cancer spheroid formed by fast fabrication method. *Vitr. Models* **3**, 19–32 (2024).
18. Soon, T. T. K. et al. Effects of Anticancer Drugs on Glia-Glioma Brain Tumor Model Characterized by Acoustic Impedance Microscopy. *Jpn. J. Appl. Phys*. **56**. https://doi.org/10.7567/JJAP.56.07JF15 (2017).
19. Franceschini, E., de Monchy, R. & Mamou, J. Quantitative characterization of tissue microstructure in concentrated cell pellet biophantoms based on the structure factor model. *IEEE Trans. Ultrason. Ferroelectr. Freq. Control* **3010**, 1–14 (2016).
20. Muleki-Seya, P. et al. High frequency quantitative ultrasound spectroscopy of excised canine livers and mouse tumors using the structure factor model. *IEEE Trans. Ultrason. Ferroelectr. Freq. Control* **3010**, 1 (2016).
21. Ayala, Y. A. et al. Effects of cytoskeletal drugs on actin cortex elasticity. *Exp. Cell Res.* **351**, 173–181 (2017).
22. Guo, M. et al. Probing the stochastic, motor-driven properties of the cytoplasm using force spectrum microscopy. *Cell* **158**, 822–832 (2014).
23. Moeendarbary, E. et al. The cytoplasm of living cells behaves as a poroelastic material. *Nat. Mater.* **12**, 253–261 (2013).
24. Watanabe, T., Hosoya, H. & Yonemura, S. Regulation of myosin II dynamics by phosphorylation and dephosphorylation of its light chain in epithelial cells. *Mol. Biol. Cell* **18**, 605–616 (2006).
25. Fadhel, M. N., Berndl, E. S. L., Strohm, E. M. & Kolios, M. C. High-frequency acoustic impedance imaging of cancer cells. *Ultrasound Med. Biol.* **41**, 2700–2713 (2015).
26. Strohm, E., Czarnota, G. J. & Kolios, M. C. Quantitative measurements of apoptotic cell properties using acoustic microscopy. *IEEE Trans. Ultrason. Ferroelectr. Freq. Control* **57**, 2293–2304 (2010).
27. Vlad, R. M. et al. An increase in cellular size variance contributes to the increase in ultrasound backscatter during cell death. *Ultrasound Med. Biol.* **36**, 1546–1558 (2010).
28. Mamou, J. & Oelze, M. L. *Quantitative Ultrasound in Soft Tissues*; 2013. https://doi.org/10.1007/978-94-007-6952-6.
29. Oelze, M. L., Zachary, J. F. & O'Brien, W. D. Characterization of tissue microstructure using ultrasonic backscatter: theory and technique for optimization using a Gaussian form factor. *J. Acoust. Soc. Am.* **112**, 1202–1211 (2002).
30. Kovács, M., Tóth, J., Hetényi, C., Málnási-Csizmadia, A. & Sellers, J. R. Mechanism of Blebbistatin Inhibition of Myosin II*. *J. Biol. Chem.* **279**, 35557–35563 (2004).

Acknowledgements

This study was partly supported by grants from the Nakatani Foundation for Advancement of Measuring Technologies in Biomedical Engineering and the JSPS KAKENHI (No.21K19893) to D.Y., and the Terumo Life Science Foundation to K. Ito.

Author contributions

D.Y. and K.Ikushima provided the initial project direction. K.Ito designed the study, conducted pre- and post- processing. K.Ito and T.M. conducted the ultrasound data acquisition. Y.I. performed the analysis of the distribution of protein fluorescence intensity, and protein quantification with Western Blotting. K.T. co-designed the study, provided technical support for the ultrasound data quantification. G.H. developed, prepared, and provided the superhydrophobic substrates for spheroid fabrication. K.Ito, Y.I., K.T. and D.Y. wrote the manuscript. All authors contributed to the final manuscript.

Competing interests

An author, K. Ikushima., serves as the CEO and shareholder of ASEMtech Inc. Although the author has received joint research funding from ASEMtech Inc., this funding is unrelated to the content of the manuscript. The other authors declare no competing interests.

Additional information

Supplementary information The online version contains supplementary material available at https://doi.org/10.1038/s44385-025-00026-w.

Correspondence and requests for materials should be addressed to Kazuyo Ito, Kenji Ikushima or Daisuke Yoshino.